nature portfolio

https://doi.org/10.1038/s41586-025-09042-7

Supplementary information

Electrochemical loading enhances deuterium fusion rates in a metal target

In the format provided by the authors and unedited

Supplementary Information for

Electrochemical loading enhances deuterium fusion rates in a metal target

Kuo-Yi Chen[1], Jannis Maiwald[1], Phil A. Schauer[1], Sergey Issinski[1], Fatima H. Garcia[1], Ryan Oldford[1], Luca Egoriti[2], Shota Higashino[1], Aref E. Vakili[1], Yunzhou Wen[1], Joseph Z. X. Koh[1], Thomas Schenkel[3], Monika Stolar[1], Amanda K. Brown[1], and Curtis P. Berlinguette[* 1,4,5,6]

[1]Department of Chemistry, The University of British Columbia, 2036 Main Mall, Vancouver, British Columbia, Canada

[2]TRIUMF, 4004 Wesbrook Mall, Vancouver, British Columbia, Canada

[3]Accelerator Technology and Applied Physics Division, Lawrence Berkeley National Laboratory, Berkeley, CA, USA

[4]Department of Chemical and Biological Engineering, The University of British Columbia, 2360 East Mall, Vancouver, British Columbia, Canada

[5]Stewart Blusson Quantum Matter Institute, The University of British Columbia, 2355 East Mall, Vancouver, British Columbia, Canada

[6]Canadian Institute for Advanced Research (CIFAR), 661 University Avenue, Toronto, Ontario, Canada

*Corresponding author: Curtis P. Berlinguette (cberling@chem.ubc.ca)

Table of contents

Supplementary Note 1: Fuel density in palladium deuteride

We calculated the fuel density in palladium deuteride (PdD) using the formula:

$$\rho_D = \frac{Z}{V}$$

where Z is the number of formula units per unit cell and V is the volume of the unit cell.

The fuel density of palladium deuteride, with a D/Pd molar ratio of 1, a unit cell volume of 68.12 $Å^3$ (68.12×10^{-30} m^3), and 4 D atoms per unit cell at 77 K is calculated as[1]:

$$\rho_D = \frac{4}{68.12\times10^{-30}\ m^3} = 5.9\times10^{28}\ m^{-3}$$

Supplementary Note 2: Mean free path in the Thunderbird Reactor

The mean free path (λ) of deuterium gas can be estimated using the following equation[2]:

$$\lambda = \left(\frac{k_B T}{\sqrt{2}\pi d^2 p}\right)$$

where k_B is Boltzmann constant, T is the temperature of the residual deuterium gas in the chamber, d is the kinetic diameter of a deuterium gas, and p is the pressure in the vacuum chamber.

We assumed the kinetic diameter of deuterium gas to be 289 pm [3], the temperature of the residual deuterium gas to be equivalent to the gas inlet temperature of 300 K, and a maximum pressure in the Thunderbird Reactor of 4×10^{-5} Torr (5.3×10^{-3} Pa). This results in a mean free path for the deuterium gas of:

$$\lambda = \frac{(1.38\times10^{-23} JK^{-1})(300\ K)}{\sqrt{2}\pi(289\times10^{-12}\ m)^2 (5.3\times10^{-3} J/m^3)} = 2.1\ m$$

At the energy scale of 10^3 eV, the kinetic diameter for $H^+ + H_2$ (momentum transfer) is 11 pm, and for $e^- + H_2$ (total interaction), it is 112 pm[4,5]. Both values are smaller than the kinetic diameter of deuterium gas, therefore, we defined the mean free path of 2.1 m as the lower bound of the mean free path.

The value of the mean free path is 30 times greater than the distance between the palladium target and the thruster outlet (6.8 cm; Supplementary Fig. 1), indicating that deuterium ions can travel unimpeded through the chamber to the target. Based on this, we assumed that any rate of fusion events in the plasma phase is negligible.

Supplementary Note 3: Reactor control software

We designed a custom reactor control and data acquisition system comprising device monitors connected to a central server via WiFi. The device monitors (e.g. Arduino MKR-1010 WiFi, Raspberry Pi Zero) were paired with reactor devices, including current meters, a mass flow controller, and a microwave generator. These monitors managed communication and data acquisition for the attached devices, ensuring synchronization using Coordinated Universal Time (UTC) for precise timestamping.

The central server operated with a Mosquitto MQTT server, a Redis database, a custom backend developed in Python/Flask, and a frontend developed in NodeJS, React, and Redux, ensuring efficient management of reactor operations and data acquisition.

Supplementary Note 4: Faradaic efficiency of D penetration through the Pd target

The Faradaic efficiency (FE%) of D loading in Pd was determined using a gas chromatograph (GC; SRI-8610C; Mandel). A palladium membrane reactor was used to conduct this experiment[6,7]. The cell consists of two chambers separated by a Pd target: an electrochemical chamber and a chemical chamber. The electrochemical chamber was filled with 2 M K_2CO_3 in D_2O to match the conditions reported in the main manuscript. The chemical chamber was filled with water to minimize headspace. Galvanostatic electrolysis was carried out in the electrochemical chamber at 133 mA cm^{-2} using a Pd foil (25 μm) as a cathode and a Pd wire as an anode. The chemical chamber was vented directly into the gas-sampling loop of a GC. The GC maintained a constant temperature of 70 °C for 3 min. A GC run was initiated every 2 min, corresponding to a sampling interval of 5 min. The GC was equipped with a packed MolSieve 5 Å column and a packed HaySep D column, and D_2 was detected on a thermal conductivity detector. D_2 evolution from the chemical chamber was monitored for 30 minutes to confirm that the flux of D_2 through the Pd reached a steady state (where the flux was relatively constant for at least 5 minutes). The electrochemical chamber was then vented to the GC, following the same sampling method, to measure the steady state of D_2 evolution in the electrochemical cell (Supplementary Fig. 2).

Any D_2 evolved from the chemical chamber would have to first absorb into the Pd target on the electrochemical chamber side. Thus, the D_2 evolving in the chemical chamber is a direct measurement for D penetration through the Pd target. The Faradaic efficiency of D penetration through the Pd was determined by comparing the total D_2 evolved from the chemical chamber to the total D_2 evolved in the experiment according to the following equation:

$$FE\% = \frac{D_{2\,chem}}{D_{2\,chem} + D_{2\,echem}} \times 100\% = \frac{3.8\times10^3}{3.8\times10^3+3.7\times10^3} \times 100\% = 51\%$$

where FE% is the Faradaic efficiency of D penetration through the Pd, $D_{2\,chem}$ is the average peak integration of D_2 evolved from the chemical chamber at steady state and $D_{2\,echem}$ is the average peak integration of D_2 evolved from the electrochemical chamber at steady state. The FE% for D loading into Pd was determined to be 51% at steady state.

Supplementary Note 5: Comparison of a Pd membrane reactor to Thunderbird Reactor

Inspired by previous work, we modified a Pd membrane reactor, originally designed for electrochemically-driven hydrogenation, to couple with the vacuum chamber at the core of the Thunderbird Reactor. In short, in the Pd membrane reactor, electrolysis occurs in a 1 M $H_2SO_{4(aq)}$ solution. Protons (H^+) generated from electrolysis are reduced to hydrogen atoms (H) at the Pd membrane, which also acts as the cathode. The H pass through the Pd membrane into the hydrogenation chamber, where they hydrogenate an unsaturated chemical bond. In the Thunderbird Reactor, electrolysis occurs in a 2 M K_2CO_3 solution in D_2O. The D_2O is then reduced to deuterium atoms (D) at the Pd target, which acts as a cathode. The D are absorbed into the Pd target, where they potentially fuse with D sourced from the ion source. A schematic comparing the two reactors is provided in Supplementary Fig. 3.

Supplementary Note 6: Neutron detection and analysis

Neutron detector

Fusion rates were observed using a single-detector neutron diagnostic system, referred to as the "EJ-309 detector". The EJ-309 detector consists of a 12.7 × 12.7 cm cylindrical cell from Eljen Technology (model: 510-50×50-9), which is filled with a liquid scintillator (EJ-309) and coupled to a Hamamatsu R1250 photomultiplier tube (PMT) encased in a Mu-metal shield (Supplementary Fig. 4).

The PMT was biased by a CAEN R1470ET high-voltage power supply. The output signal from the PMT was directly sampled and digitized with a 14-bit 500 MHz CAEN DT5730S waveform digitizer equipped with DPP-PSD firmware. To balance between maximizing the effective number of digitizer bits and fitting spectral features of neutron energies up to 5 MeV, the expected maximum pulse height that would correspond to 2.45 MeV neutron signal was positioned near the digitizer's input midrange. This alignment was accomplished by applying a PMT bias voltage of –1525 V. The neutron data were collected using CAEN CoMPASS software[8].

Detector response to neutrons and gamma rays

The EJ-309 scintillator is filled with scintillation liquid (Eljen Technology; NEUTRON/GAMMA PSD EJ-309). When excited by incident particle interaction, the liquid scintillator molecules become heated (vibrational excitation) and/or excited (electronic excitation). When these molecules relax to a ground state, photons in the visible spectrum are emitted by photoluminescence at around 10^{-9} s. The amount of light produced, known as the light output, is measured in keVee (kilo-electron volt equivalent). The light output is proportional

to the type of incident particle and the amount of energy deposited into the scintillator. The amount of light produced by a 1 MeV gamma ray differs from that produced by a 1 MeV neutron due to the distinct interaction mechanics with the scintillator. Gamma rays primarily deposit their energy in the detector through Compton scattering because the EJ-309 scintillator is composed of low atomic number elements like carbon and hydrogen. On the other hand, neutrons in the 1–5 MeV range deposit energy mainly through elastic scattering with hydrogen[9]. These different interactions result in a characteristic pulse height spectrum, referred to as the gamma-ray response and the neutron response[10].

Electric noise mitigation

Electrical noise was minimized by matching impedances between the PMT and the digitizer. An RG316 coaxial cable (length: 1.83 m; purchased from CD International Technology) was used between the detector and the digitizer. The noise floor was suppressed by setting the signal amplitude threshold in the CoMPASS software to 250 least significant bits, which corresponds to 43 keVee.

Pileup rejection

If two or more particles hit the detector at the same time, they can cause a pileup of multiple signals in a single acquisition window. Given an acquisition window of 400 ns, a detector-source distance of 12 cm, and the Thunderbird Reactor yield rate of 54 kHz, the contribution from these pileup events was measured to be 4.8% of the total neutron count rate. By setting the PUR-GAP filter[8] in CoMPASS to 100 LSB we reduced the pileup events in the final dataset to <1%.

Magnetic shielding

The magnetic field generated by the permanent magnets in the thruster significantly interferes with the PMT of the EJ-309 detector. This magnetic field deflects the trajectories of the photoelectrons and electrons within the PMT region, resulting in poor detection efficiency and a degraded pulse height spectrum. The strength of the magnetic field was reduced from 40 Gauss to <0.3 Gauss at the front of the detector by placing the detector inside a double-layer magnetic shield manufactured from Mu-metal and Co-NETIC (Supplementary Fig. 4). The external layer of the shield is 57.6 cm long and has a radius of 10.54 cm, the internal layer is 55.1 cm long and has a radius of 9.30 cm.

The effectiveness of the shielding was experimentally verified by comparing the Compton edge position of the ^{40}K isotope with the literature value. The Compton edge (L; measured in keVee) is calculated by:

$$L = 2\left(\frac{E_\gamma^{\,2}}{2E_\gamma + 511}\right)$$

where E_γ is the energy of the incident gamma-ray photon measured in keV, and 511 keV is the rest energy mass of the electron.

The position of the Compton edge was determined by taking the first derivative of the detector response function as described by Safari[11]. The literature gamma-ray energy peak of ^{40}K was precisely measured to be 1461 keV[12]. This value can be converted to a Compton edge by:

$$L = 2\left(\frac{(1461\ keV)^2}{2(1461\ keV) + 511\ keV}\right) = 1243\ keVee$$

Our measured Compton edge of 1270 keVee is different by less than 3% of the calculated Compton edge of ^{40}K, 1243 keVee.

Particle discrimination

The EJ-309 detector is capable of detecting both neutrons and gamma rays. The two types of radiation were distinguished from each other by charge integration. Charge integration is a pulse shape discrimination technique that captures the different scintillation decay times in the EJ-309 detector[13]. The decay time for gamma-ray interactions is faster than for neutron interactions[14]. A pulse shape discrimination (PSD) variable was constructed by calculating the ratio of the integrals of the "tail" and "total" gates. The tail gate refers to a portion of the decay of the pulse after the pulse peak, while the total gate encompasses the entire pulse (Supplementary Fig. 5a)[15,16].

Counting window construction

A neutron counting window (Supplementary Fig. 5b) was constructed in the following way:

The PSD plot was cut into slices of an equal width of 5 keVee. This was conducted for the entire distribution of 0–1600 keVee. The gamma-ray peak was then fit using a Gaussian distribution to determine its mean, μ, and standard deviation, σ (Supplementary Fig. 5c).

a. The lower PSD boundary of the counting window was then set as $\mu + 5\sigma$, similar to the method used by Baramsai *et al.*[17].
b. The upper boundary was defined by adding an arbitrary 0.2 PSD units to the lower boundary.
c. The left boundary was chosen at 50 keVee as a practical estimate near the observable edge of the PSD distribution, though the analysis does not strictly depend on this threshold.

Neutron Energy Estimation

The energy of the counted neutrons was estimated through a two-step process: First, a calibration curve was built to convert the measured signal into light output of the EJ-309 liquid scintillator by using ^{60}Co, ^{137}Cs, and ^{152}Eu gamma-ray radioactive sources (Supplementary Fig. 6)[18].

Second, the experimental neutron response was compared with the simulated response generated using the Monte Carlo N-Particle (MCNP6.2)[19] and Geant4 transport codes[20–22]. The simulations specifically modeled the energy deposition within the EJ-309 scintillation liquid. A point source with a peak energy of 2.45 MeV, representative of neutrons produced in D-D fusion, was simulated using a Gaussian energy distribution with a standard deviation of 0.05 MeV to accurately model the characteristics of a physical source that emits 2.45 MeV neutrons[23]. The source was positioned 0.12 m from the front surface of the EJ-309 scintillator, following the methodology of Bai *et al.*[24]. The resolution of the detector was accounted for by incorporating a resolution function derived from Enqvist *et al*.[10].

The Detector Response Function Toolkit (DRiFT) toolkit[25] was utilized alongside MCNP6.2 to convert the simulated energy deposited by recoil protons in the scintillator (measured in keV) into a neutron response distribution (measured in keVee) (solid blue line; Supplementary Fig. 7a). These simulation results were validated with a light output analytic code written in Python that was utilized alongside Geant4 (solid blue line; Supplementary Fig. 7b). The comparison of the experimentally observed and simulated neutron responses demonstrates a reasonable agreement, with overlapping and matching trends in the response functions from 200 to 1000 keVee (Supplementary Fig. 7a). The simulated responses were scaled to match the measurements by normalizing to the maximum count in the measured spectra. The discrepancy

observed below 200 keVee is attributed to the lower PSD boundary excluding a subset of neutron events due to diminished PSD separation at low energies, effectively truncating the reliable neutron spectrum. The simulation was performed using 10^7 neutrons (estimated error is 0.03%), which provides sufficient statistics at energies up to 1000 keVee. Note that very few counts are experimentally observed beyond 1000 keVee. In order to produce those neutrons, the simulation would have to simulate many more interactions than those currently used.

Neutron Spectrum Unfolding

The neutron energy spectrum from the Thunderbird Reactor was reconstructed using the GRAVEL iterative unfolding algorithm[26]. The inputs to this algorithm are the measured neutron response (Supplementary Fig. 7b) and a detector neutron response matrix modeled with Geant4 (Supplementary Fig. 7c). A Python program that implements the GRAVEL algorithm was developed and validated for accuracy against Geant4-simulated detector responses for D-D fusion beam (Supplementary Fig. 7d). Neutron energy and counting uncertainties at the 3σ confidence were estimated using the perturbation method[27].

The unfolded spectrum of experimental results confirms that neutrons emitted from the Thunderbird Reactor closely match theoretical predictions for D-D fusion at 2.45 MeV (Supplementary Fig. 7e). In this case, the counting uncertainty was estimated as a range for three experiments presented in this study.

Supplementary Note 7: Monte Carlo simulations for the behavior of deuterium ions

The behavior of deuterium ions in Pd was simulated by the TRIM (Transport of Ions in Matter) module of the SRIM (Stopping and Range of Ions in Matter) Monte Carlo software[28]. We modeled 1×10^4 deuterium ions at 30 keV incident on a 4000 Å Pd target (400 nm). Results provide insight into penetration depth, ion distribution, and spatial behavior of deuterium in the palladium target (Supplementary Fig. 9a).

The 2D ion range profile shows ions concentrating around a projected range of 1800 Å, with a 635 Å straggle, which is the standard deviation from the maximum penetration depth. The distribution's slight asymmetry (skewness = −0.160) and sharper peak (kurtosis = 2.667) suggest localized energy transfer with minimal penetration beyond 3000 Å (Supplementary Fig. 9b).

Supplementary Note 8: Evidence for lattice confinement fusion

An experiment to test whether the fusion events were occurring inside the lattice rather than in the gas phase was conducted by cycling the sheath voltage (Extended Data Fig. 1). The 'on' periods in this experiment were characterized by applying the sheath voltage (–30 kV) between the vacuum chamber and the target, accelerating D^+ ions into the target. During the 'off' periods, the sheath voltage was turned off, such that no more D^+ ions were implanted into the target. We began the experiment by using an annealed target and performing a typical beam-loading experiment (not shown) until the neutron production rates stabilized. We define stability as the period during which all data points remain within ±5% of their mean value over a 30-min interval following the application of high voltage. Once stability was reached, we turned off the sheath voltage for 5 minutes and then turned it back on for 10 minutes. This on-off cycle was repeated three times. At the first 'off' period, we observed a decrease in the neutron production rate, returning to background levels (0.21(9) n s^{-1}). At the first 'on' period, we observed an immediate increase in the neutron production rate, stabilizing at 184.1(7) n s^{-1} rather than the gradual increase expected at the beginning of a typical beam loading cycle. The same behavior was noted in the subsequent on-off cycles. The result indicates that the concentration of deuterium in the Pd target reached a saturation value during the first beam loading instance, and the concentration remained constant as the beam loading cycles were repeated.

In-situ XRD experiments (see Methods, *In situ XRD characterization of palladium targets*) validate that the deuterium remains in the metal lattice for a prolonged period of time, indicating there is negligible loss of deuterium in the Pd target while the sheath voltage is turned off. This demonstrates that after reapplying the sheath voltage, deuterium does not need to accumulate in the Pd metal lattice again; it can fuse with the deuterium already present in the Pd

target. This is evidence that high-energy deuterium ions collide with deuterium within the Pd lattice, triggering D-D fusion rather than fusion reactions occurring with deuterium in the gas phase.

Supplementary Note 9: The effect of H_2O contamination on the neutron production rate

The effect of H_2O contamination on the neutron production rate was determined using the same experimental design as our other fusion experiments (see *Fusion reactions in the Thunderbird Reactor*) with a 2 M K_2CO_3 in H_2O electrolyte instead of D_2O. After the electrochemical cell was activated (Phase II; Extended Data Fig. 2), the neutron production rate decreased by 88.3(3)% compared to the rate observed in Phase I.

The residual gas analyzer (RGA; Methods, Vacuum chamber) was used to measure the change in the partial pressure of HD (m/q = 3) (Supplementary Fig. 13), which is defined as:

$$\Delta P_{HD}\% = \frac{P_{HDf} - P_{HDi}}{P_{HDi}} \times 100\%$$

We used this equation to quantify the degree of H_2O contamination before and after activation of the electrochemical cell. Here, P_{HDi} is the HD partial pressure 1 minute before the activation of the electrochemical cell, and P_{HDf} is the HD partial pressure 1 hour after the activation of the electrochemical cell. For Target 1 (Supplementary Fig. 13), as an example, the change in the partial pressure of HD is:

$$\Delta P_{HD}\% = \frac{2.78\times10^{-7}\,Torr - 1.24\times10^{-7}\,Torr}{1.24\times10^{-7}\,Torr} \times 100\% = 125\%$$

The ΔP_{HD} of targets 1–3 are 125%, 269%, and 106%, respectively. These ΔP_{HD} values are inversely correlated with the neutron production rate gains for each target, which are 15%, 11%, and 18%, respectively.

Supplementary Note 10: Deuterium consumption rate in a palladium target during a fusion reaction

The fraction of D that undergoes fusion is much lower than the number of D electrochemically loaded into the Pd target. The moles of D in an electrochemically loaded Pd target whose D/Pd ratio is 0.7 (see *In situ XRD characterization of palladium targets*) are given by:

$$mol = \frac{0.7\rho V}{M}$$

where ρ is is the density of Pd (12.007 g/cm^3), V is the volume of the Pd target (0.045 cm^3; calculated by the area exposed to the electrolyte of 1.5 cm^2 and the thickness of Pd target of 300 μm), and M is the atomic mass of Pd (106.42 g/mol). The moles of deuterium in the Pd target with a D/Pd ratio of 0.7 are give by:

$$mol = \frac{0.7\times12.007\times0.045}{106.42} = 3.6\times10^{-3}\,mol$$

The fraction of D atoms that result in fusion per second can be estimated from the fusion yield of 10523 fusion events/s at a sheath voltage of −30 kV and a plasma current of 0.5 mA (Supplementary Note 11). One deuterium atom in the Pd target results in a single fusion event that produces one neutron by the probability of 50%. Thus the fraction of D atoms that undergo fusion per every second is expressed as:

$$mol/s = \frac{10523\times2}{N_A}$$

where N_A is Avogadro's constant, 6.02×10^{23} mol^{-1}. The fraction of D atoms that undergo fusion per second is:

$$mol/s = \frac{10523\times2}{6.02\times10^{23}} = 3.5\times10^{-20}\,mol/s$$

If we assume that no D escapes the target, the time required to consume D in the PdD target through D-D fusion reaction is:

$$\frac{3.6\times10^{-3}\,mol}{3.5\times10^{-20}\,mol/s} = 1.0\times10^{17}s$$

Therefore, the electrochemical loading of Pd produces on the order of 10^{17} times more deuterium than is consumed per second by the fusion reaction.

Supplementary Note 11: Fusion energy gain factor Q of the Thunderbird Reactor

The fusion yield *Y* of the Thunderbird Reactor can be estimated using the formula:

$$Y = 2N \frac{4\pi}{\varepsilon_{in}\,\Omega}$$

where 4π is the total solid angle of a sphere (in steradians), *N* is the number of detected neutrons, ε_{in} is the intrinsic efficiency of the detector, and Ω is the solid angle covered by the detector (in steradians). The factor of 2 accounts for our measurement of only one of the two equally probable D-D fusion pathways, as our experiment detects only neutrons, which represent half of the total fusion yield.

We assumed a point source in front of a right circular cylindrical detector:

$$\Omega = 2\pi\left(1 - \frac{d}{\sqrt{d^2+r^2}}\right)$$

where *d* is the source-detector distance and *r* the detector radius[29].

At a source distance of 0.12 m from the detector and a detector radius 0.0635 m, the solid angle is:

$$\Omega = 2\pi\left(1 - \frac{0.12m}{\sqrt{(0.12\ m)^2+(0.0635\ m)^2}}\right) = 0.73\ sr$$

The intrinsic efficiency of our detector is 54% [30]. At a sheath voltage of −30 kV and a plasma current of 0.5 mA we detected a maximum neutron rate of $N = 165$ n s^{-1}, which results in a fusion yield of:

$$Y = 2 \times 165\ n\ s^{-1}\ \frac{12.57\ sr}{0.54 \times 0.73\ sr} = 10523\ fusion\ events/s$$

We calculated the average energy per each D-D fusion reaction:

$$E_{reac}(J) = E_{reac}(MeV) \cdot C_{eV-J}$$

where $E_{reac}(MeV)$ is the average energy per D-D fusion reaction in units of megaelectronvolts and C_{eV-J} is the conversion factor from electronvolt to Joule ($1.6\times10^{-19}\frac{J}{eV}$).

The average energy released per each D-D fusion reaction is $3.65\ MeV$:

$$E_{reac} = (3.65\,MeV)(1.6\times10^{-19}\tfrac{J}{eV}) = 5.84\times10^{-13}J$$

The total power output P_{out} of the reactor is calculated as:

$$P_{out} = Y \cdot E_{reac}$$

$$P_{out} = (10523\,s^{-1})(5.84\times10^{-13}J) = 6.15\times10^{-9}\,\tfrac{J}{s}.$$

The power input of the reactor is calculated as:

$$P_{in} = V_S \cdot I_P$$

where V_S is the sheath voltage and I_S is the plasma current.

$$P_{in} = (30\,kV)(0.5\,mA) = 15\,\tfrac{J}{s}$$

The fusion gain factor Q is obtained as:

$$Q = \frac{P_{out}}{P_{in}}$$

$$Q = \frac{6.15\times10^{-9}\,\frac{J}{s}}{15\,\frac{J}{s}} = 4.1\times10^{-10}$$

The extra energy gain (ΔQ) in neutron production obtained by electrochemical loading of deuterium in the Pd target is defined as;

$$\Delta Q = Q' - Q = \frac{P_{out}+\Delta P_{out}}{P_{in}+\Delta P_{in}} - \frac{P_{out}}{P_{in}}$$

where Q' is the fusion gain factor after electrochemical loading, ΔP_{out} is the gain in the total power output of the reactor, and ΔP_{in} is the gain in the total power input of the reactor.

ΔP_{in} is calculated as:

$$\Delta P_{in} = V_E \cdot I_E = (3.8\,V)(200\,mA) = 0.76\,\tfrac{J}{s}$$

where V_{E} is the voltage of the electrochemical cell, and I_{E} is the current of the electrochemical cell (Supplementary Fig. 19).

ΔP_{out} is calculated as:

$$\Delta P_{out} = 0.15 P_{out} = 0.15(6.15\times10^{-9}\ \frac{J}{s})$$

for the experiment where the neutron production rate increased by 15% as a result of electrochemically loading the Pd target.

ΔQ is calculated as:

$$\Delta Q = \frac{6.15\times10^{-9}\ \frac{J}{s} + 0.15(6.15\times10^{-9}\ \frac{J}{s})}{15\ \frac{J}{s} + 0.76\ \frac{J}{s}} - \frac{6.15\times10^{-9}\ \frac{J}{s}}{15\ \frac{J}{s}} = 3.87\times10^{-11}$$

The positive value of ΔQ indicates that the electrochemical loading of Pd produces a net energy gain.

Supplementary Figures

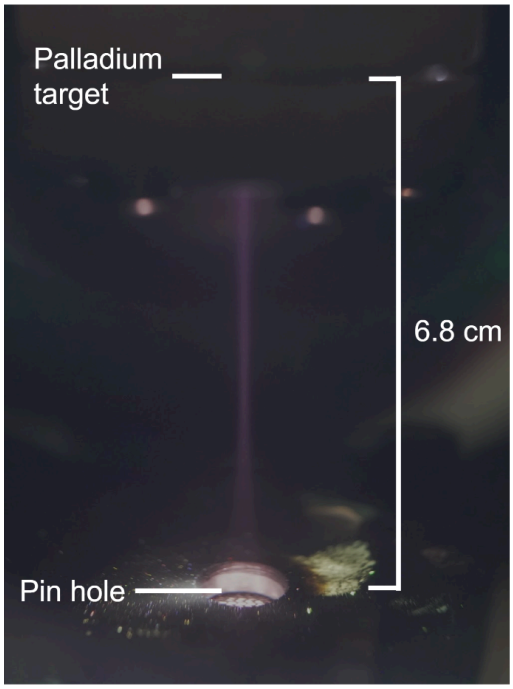

Supplementary Fig. 1: Pin hole placement in the Thunderbird Reactor. Plasma expelled from the plasma thruster below the pin hole travels upwards to the palladium target, where fusion events occur.

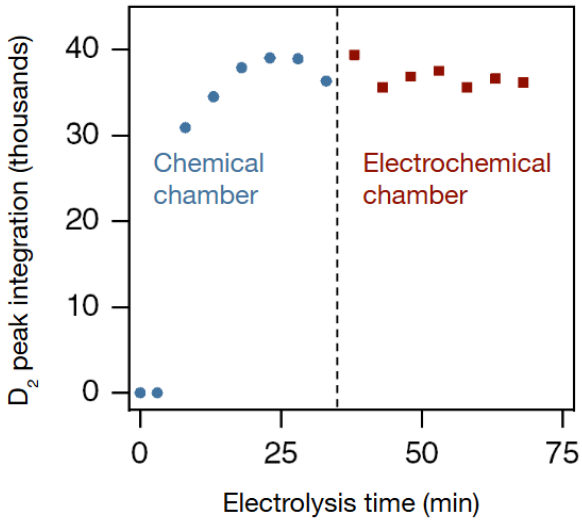

Supplementary Fig. 2: Representative D_2 flux in the Thunderbird Reactor. D_2 peak integration vs time as measured by a gas chromatograph (GC). A two-chamber cell, composed of electrochemical and chemical chambers, equivalent to the Thunderbird Reactor, was used. Galvanostatic electrolysis was carried out in the electrochemical chamber filled with 2 M K_2CO_3 in D_2O at 133 mA cm^{-2} using a Pd foil (25 μm) as the cathode throughout the experiment. During the initial 30 min (blue circles, left of the dotted line), D_2 evolution from the chemical chamber was monitored until saturation. After 30 min (red squares, right of the dotted line), D_2 evolution from the electrochemical chamber was monitored.

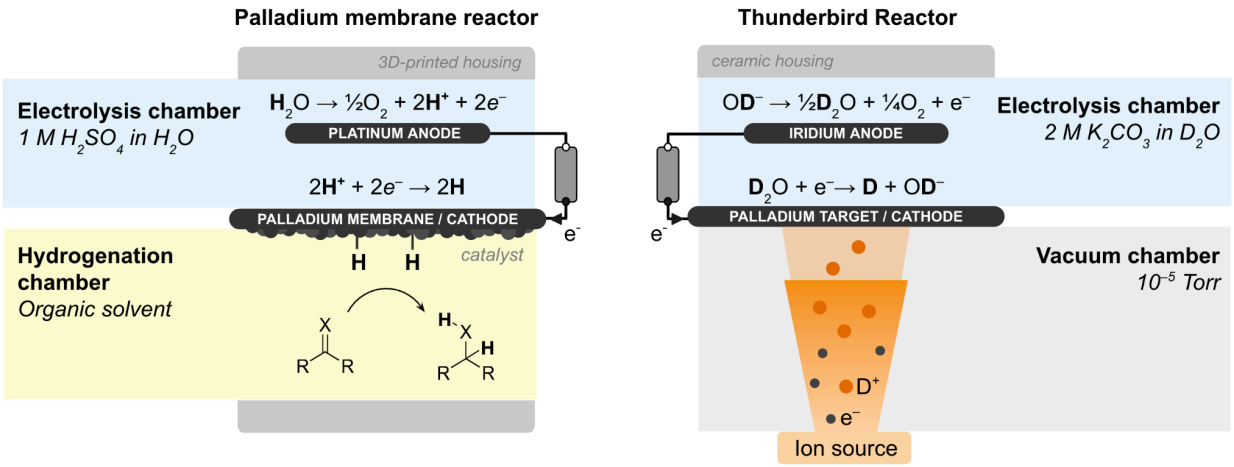

Supplementary Fig. 3: Illustrative comparison of a Pd membrane reactor and the Thunderbird Reactor. In the Pd membrane reactor, electrolysis occurs using a 1 M $H_2SO_{4(aq)}$ solution. Water is oxidized into protons (H^+) and oxygen gas ($O_{2(g)}$) at the platinum anode. The H^+ migrate to the palladium membrane where they are reduced to hydrogen atoms (H) at the palladium membrane, which also acts as the cathode. The H pass through the Pd membrane into the hydrogenation chamber, where they hydrogenate an unsaturated chemical bond. A high surface area catalyst on the Pd membrane, facing the hydrogenation chamber, facilitates the hydrogenation reaction. In the Thunderbird Reactor, electrolysis occurs in a 2 M K_2CO_3 solution in D_2O. Deuteroxide (OD^-) is oxidized into D_2O and $O_{2(g)}$ at the iridium anode. The D_2O is then reduced to deuterium atoms (D) at the Pd target, which acts as a cathode. The D are absorbed into the Pd target, where they potentially fuse with D sourced from the ion source.

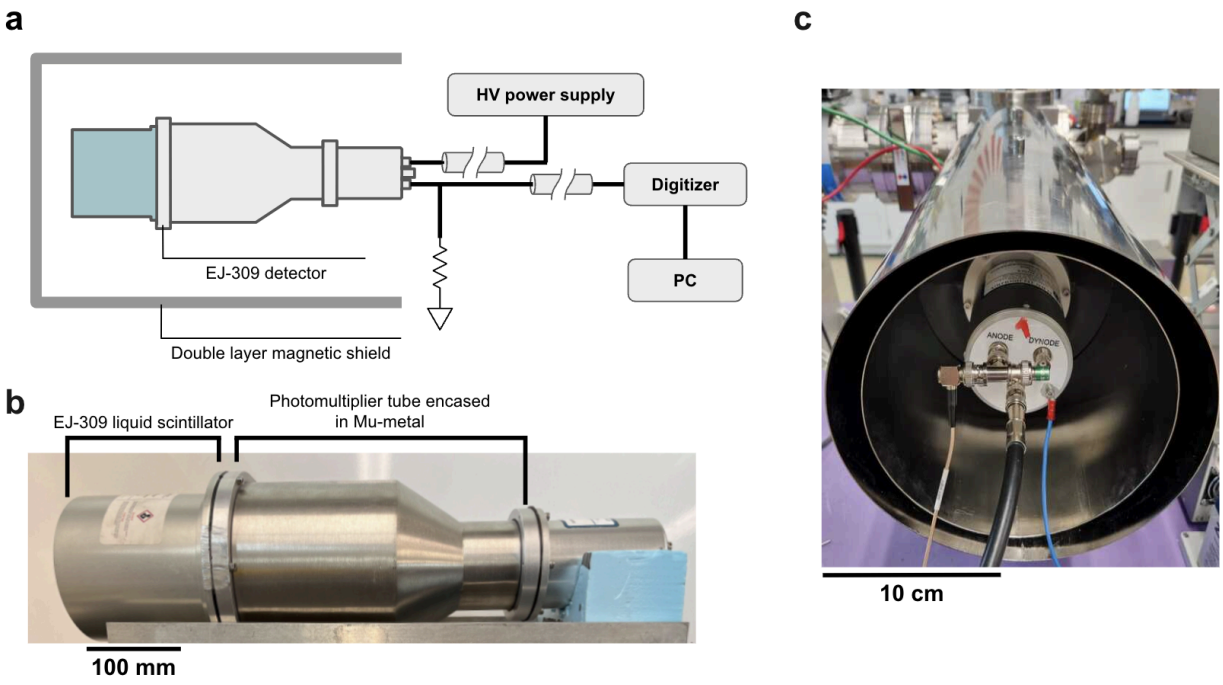

Supplementary Fig. 4: Neutron detector capabilities within the Thunderbird Reactor. a, Schematic illustrating the neutron detection system as a part of the Thunderbird Reactor, highlighting key components of the system. **b,** A photo of the EJ-309 detector. **c**, EJ-309 detector, shown from the back, inside the double-walled magnetic shielding composed of Mu-metal and Co-NETIC materials.

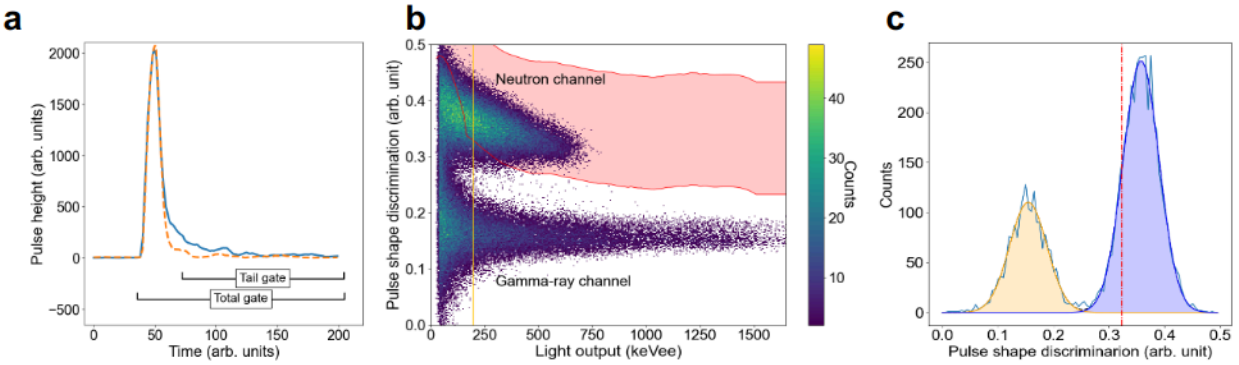

Supplementary Fig. 5: Particle discrimination within the Thunderbird Reactor. a, Sample waveforms, showing the difference between gamma-ray signals (dashed orange line) and neutrons (solid blue line). The "tail gate" refers to the portion of the waveform after pulse decay, while the "total gate" refers to the entire waveform. The ratio between the two is used to construct the pulse shape discrimination value. **b,** The result of neutron and gamma-ray discrimination. The red border outlines the neutron counting window. The vertical yellow line shows the location of a sample energy slice. **c,** Cross-section view of a sample energy slice, fit with two Gaussian distributions. The gamma-ray channel is in yellow, and the neutron channel is in blue. The red dashed line indicates the 5σ cutoff from the gamma-ray distribution. The region to the right of this line will include only 0.00006% of detected gamma rays.

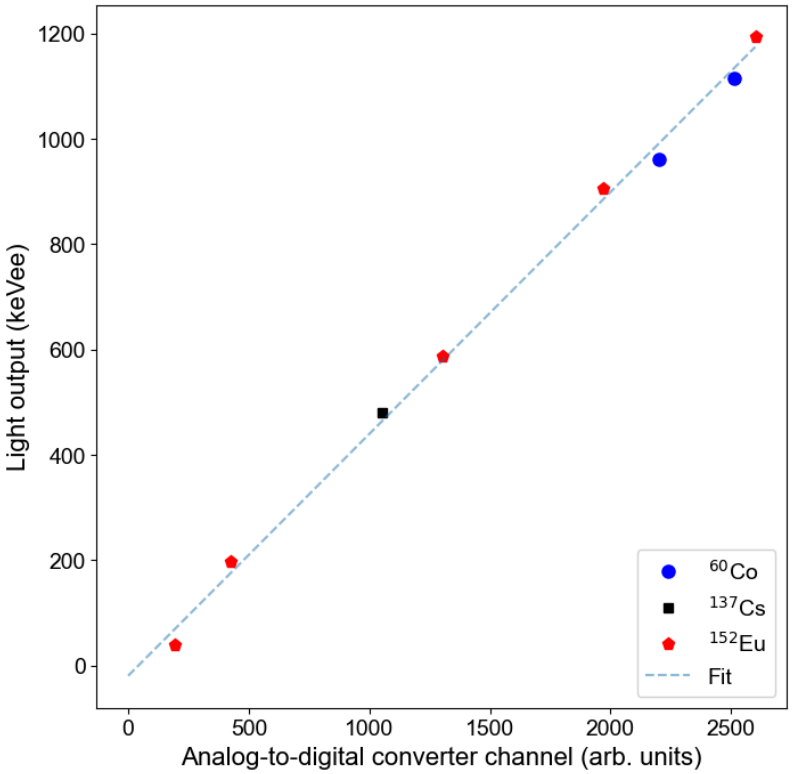

Supplementary Fig. 6: Energy calibration curve for the EJ-309 detector. The fit is linear (y = a (x) + b) with coefficients: a = 2.179, b = 41.57.

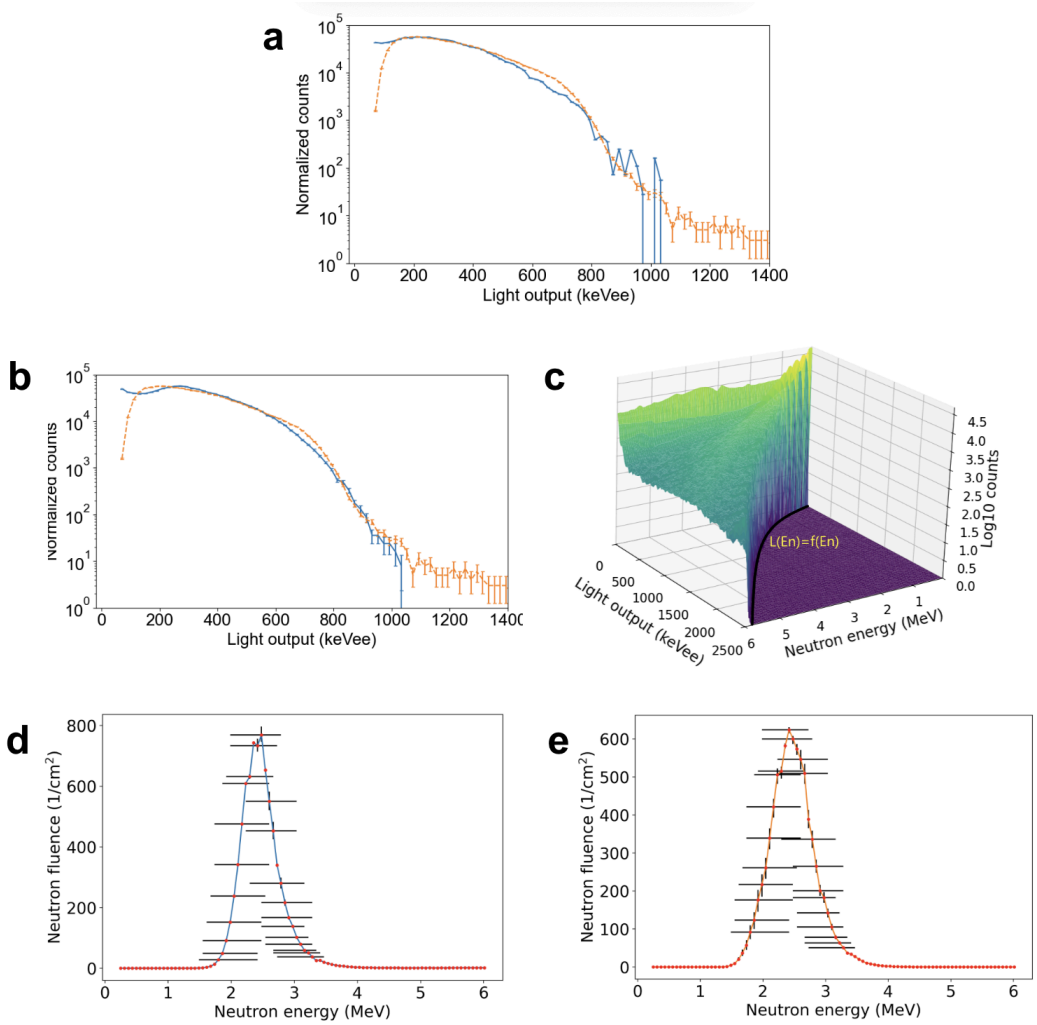

Supplementary Fig. 7: Spectroscopy of neutrons produced by the Thunderbird Reactor. a, b, Comparison of the measured neutron response from the Thunderbird Reactor (dashed orange line) and the simulated (a, MCNP6.2 and b, Geant4) neutron response for the EJ-309 detector from a D-D fusion neutron source (solid blue line). **c**, Simulated in Geant4 EJ-309 detector response matrix constructed with neutron energy steps of 62 keV. **d**, Unfolded spectrum of the simulated in Geant4 response for a D-D fusion neutron beam with Gaussian-like shape and a standard deviation of 0.05 MeV, similar to what is expected for a D-D reaction with kinetic energy of 30 keV[23]. The simulated counts were scaled to match experimental counts. These results validate the Python code implementation of the GRAVEL spectrum unfolding algorithm. Fluence uncertainty is presented as the square root of fluence, while energy uncertainty is calculated using the perturbation method[27]. **e**, Unfolded spectrum of neutrons produced by the Thunderbird Reactor. The result was averaged across three 2-hour experimental campaigns where electrochemical loading was used (Fig. 3), validating consistency with the expected D-D fusion reaction spectrum.

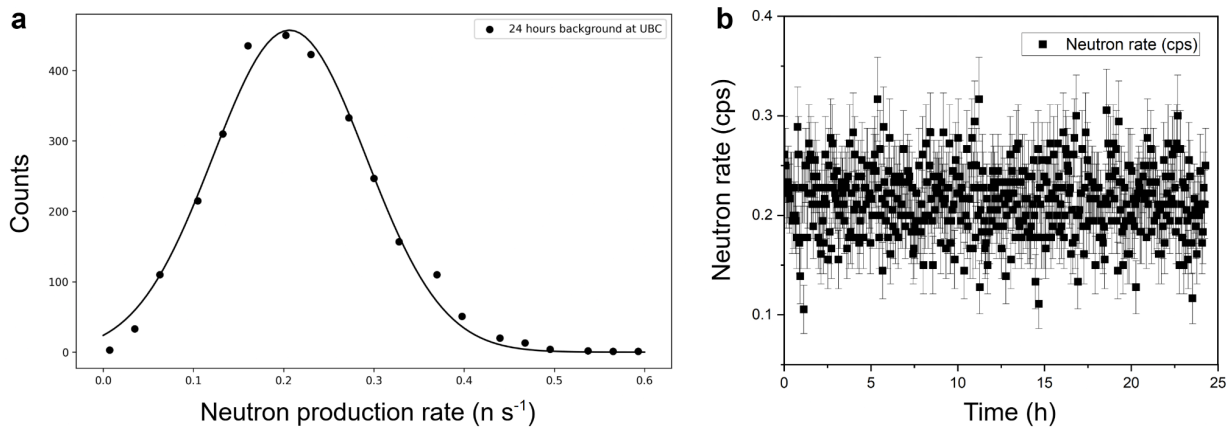

Supplementary Fig. 8: 24-Hour neutron background at the University of British Columbia (UBC). **a,** The 24-hour neutron background value measured at UBC is 0.21(9) n s^{-1}. **b,** 24-Hour neutron background vs time. Data are presented as mean ± s.d., with a dwell time of 180 seconds. The neutron rate from the Thunderbird Reactor during a typical experiment (Fig. 3) is more than 650 times higher than the background rate.

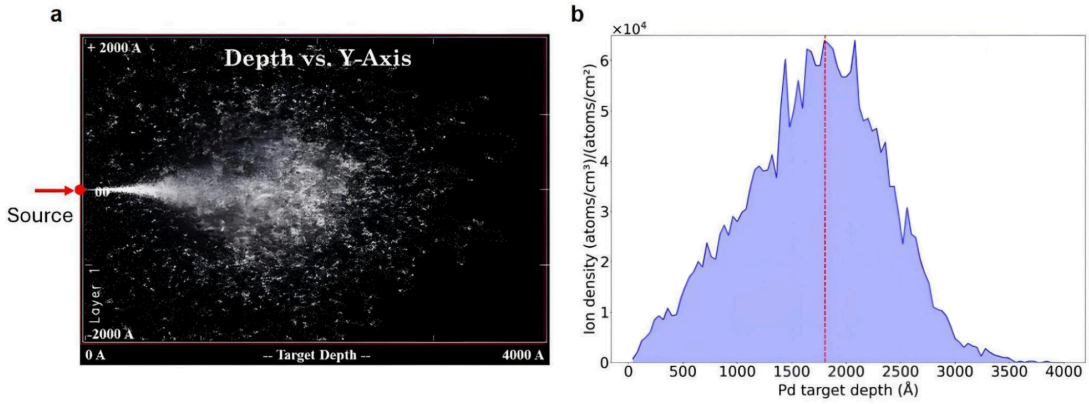

Supplementary Fig. 9: Model of 30 keV deuterium penetration into a palladium target. a, The 2D profile of deuterium penetration, showing ions emitted from the left (source) and their implantation distribution across the Pd target obtained using the TRIM package of SRIM. White points indicate ion concentration and interaction patches. **b**, Depth distribution highlighting the penetration peak at around 1800 Å, where ion implantation is most concentrated at the dotted red line denoted as "ion range". Parameters: Straggle = 635 Å; skewness = −0.160; and kurtosis = 2.667.

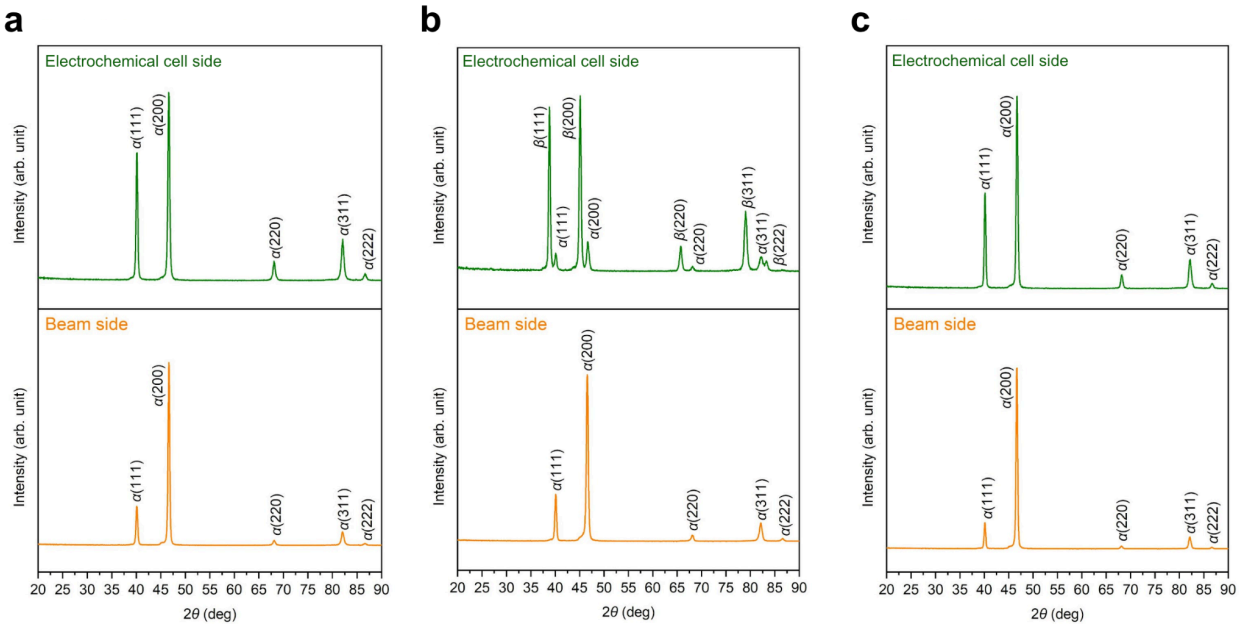

Supplementary Fig. 10: XRD spectra of a sample Pd target. a, XRD spectra of a Pd target prior to the fusion experiment. **b**, XRD spectra of a Pd target after the fusion experiment. **c**, XRD spectra of a Pd target after annealing. The fusion experiment included beam loading for 60 min with a sheath voltage of −30 kV and a plasma current of 0.5 mA and electrochemical loading for 60 min with a constant current of 200 mA across the electrochemical cell. The target was annealed at 400 °C for one hour at 10^{-5} Torr. XRD spectra were taken on both sides of Pd targets; the side exposed to the electrolyte in the electrochemical cell (denoted as "electrochemical cell side") and the other exposed to the D^+ beam in the vacuum chamber (denoted as "beam side").

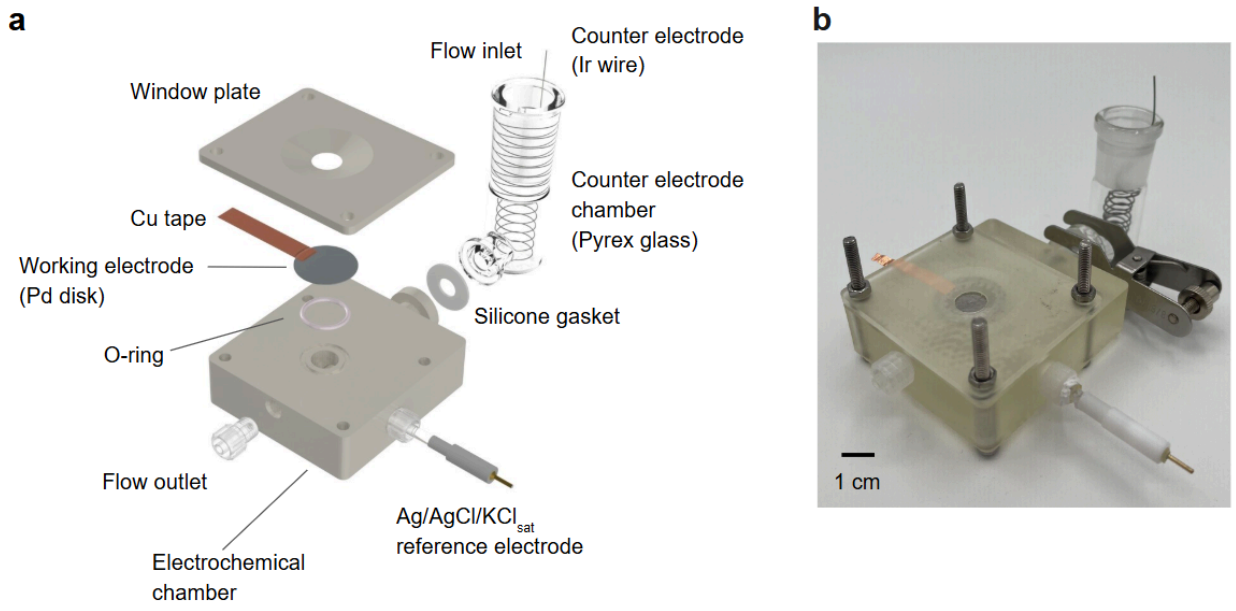

Supplementary Fig. 11: Electrochemical cell for *in situ* XRD experiments. a, CAD illustration of the 3D printed electrochemical cell for *in situ* XRD measurement. **b**, Photograph of the assembled electrochemical cell for *in situ* XRD measurement. A Pd target was sandwiched between the electrochemical chamber and a window plate. A strip of a Cu tape was attached to the Pd target as the electrical contact. The interface between the Pd target and the electrochemical cell was sealed using a Viton™ fluoroelastomer O-ring, exposing 1.5 cm^2 of the Pd target to the electrolyte, the same area as in the Thunderbird Reactor. The electrochemical chamber, Pd target, and window plate were clamped together using four M4 stainless steel screws. A counter electrode chamber made of pyrex glass was attached to the electrochemical cell using a stainless clamp and a silicone gasket for sealing. A 25 cm long Ir wire (0.5 mm, 99.95%) was formed into a screw shape and used as the counter electrode. An $Ag/AgCl/KCl_{sat}$ reference electrode was inserted near the Pd target through a hole in the electrochemical chamber. The electrolyte was circulated by using a Kamoer LLS Plus V2 peristaltic pump at a flow rate of 100 mL/min through the electrochemical cell.

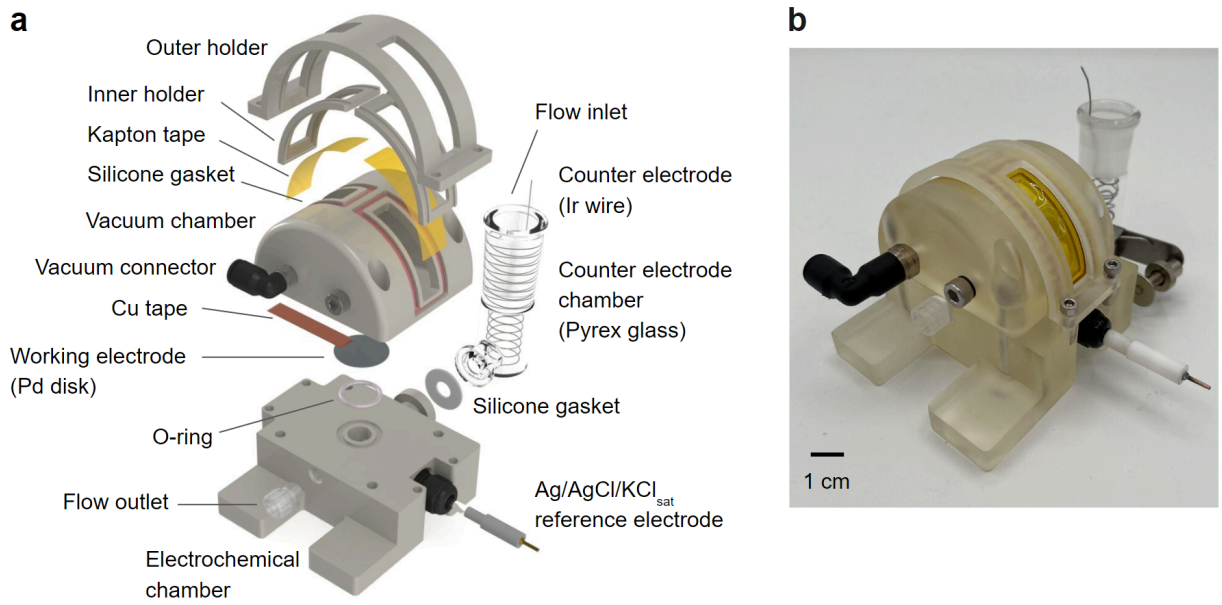

Supplementary Fig. 12: Electrochemical cell for *in situ* XRD experiments in vacuum. a, CAD illustration of the 3D printed electrochemical cell for *in situ* XRD measurement in vacuum. **b**, Photograph of the assembled electrochemical cell for *in situ* XRD measurement. A Pd target was sandwiched between the electrochemical chamber and a vacuum chamber. The vacuum chamber was sealed with semicircular-shaped frames that hold 25.4 µm-thick Kapton tapes as an X-ray transparent window. The vacuum chamber was connected to an Edwards E2M5 rotary pump through a vacuum connector and a PTFE tube to achieve 1.2×10^{-2} Torr. A strip of a Cu tape was attached to the Pd target as the electrical contact. The interfaces between the Pd target and the electrochemical and vacuum chambers were sealed using a Viton™ fluoroelastomer O-ring. 1.5 cm^2 of the Pd target, the same area as in the Thunderbird Reactor, was exposed to the electrolyte. The electrochemical chamber, Pd target, and vacuum chamber were clamped together using four M4 stainless steel screws. A counter electrode chamber made of pyrex glass was attached to the electrochemical cell using a stainless clamp and a silicone gasket for sealing. A 25 cm long Ir wire (0.5 mm, 99.95%) was formed into a screw shape and used as the counter electrode. A $Ag/AgCl/KCl_{sat}$ reference electrode was inserted near the Pd target through a hole in the electrochemical chamber. The electrolyte was circulated by using a Kamoer LLS Plus V2 peristaltic pump at a flow rate of 100 mL/min through the electrochemical cell.

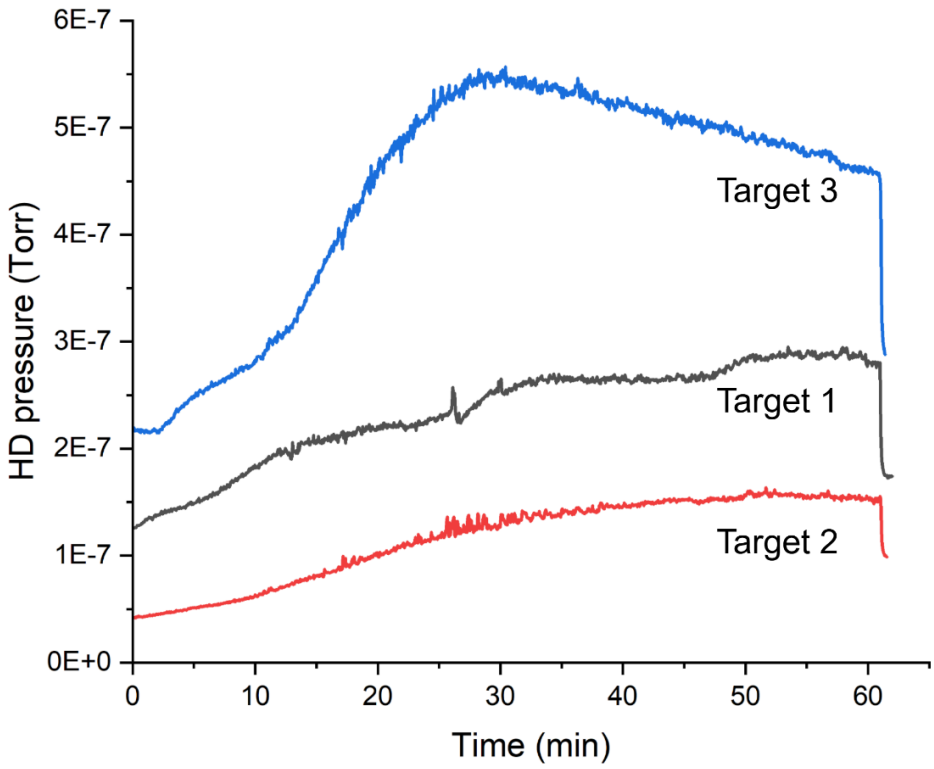

Supplementary Fig. 13: HD partial pressure in the vacuum chamber after activation of the electrochemical cell (Phase II of the fusion experiment). A residual gas analyzer is used to monitor the HD (m/q = 3) partial pressure change in the vacuum chamber after activation of the electrochemical cell, where H comes from water pollution in the electrochemical cell. The ΔP_{HD} of targets 1–3 (Fig. 3) are 125%, 269%, and 106%, respectively (Supplementary Note 9).

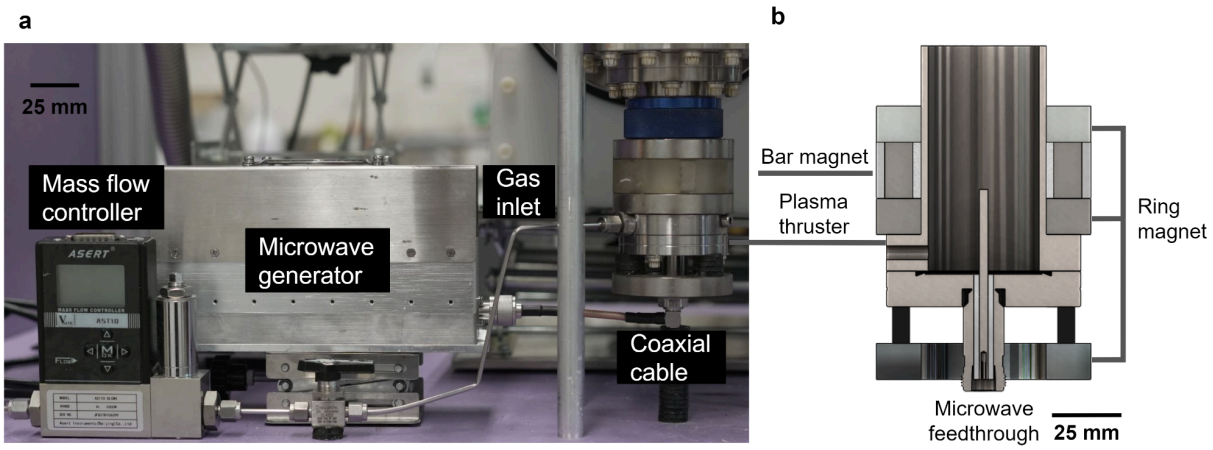

Supplementary Fig. 14: The plasma thruster of the Thunderbird Reactor. a, Photograph of the plasma thruster setup, showing the individual components required to operate the plasma thruster. **b**, CAD illustration of the cross-section of the plasma thruster.

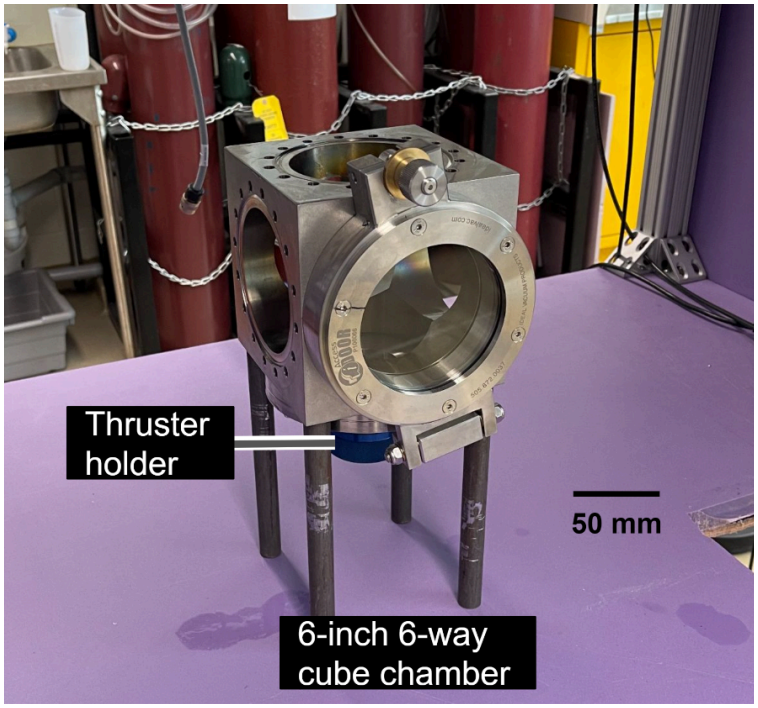

Supplementary Fig. 15: The vacuum chamber of the Thunderbird Reactor. A 6-inch, 6-way standard CF flange cube is at the center of the reactor. Its primary function is to physically connect the electrochemical cell and the plasma thruster while providing an appropriate vacuum environment for the operation of the plasma thruster and plasma immersion ion implantation (PIII).

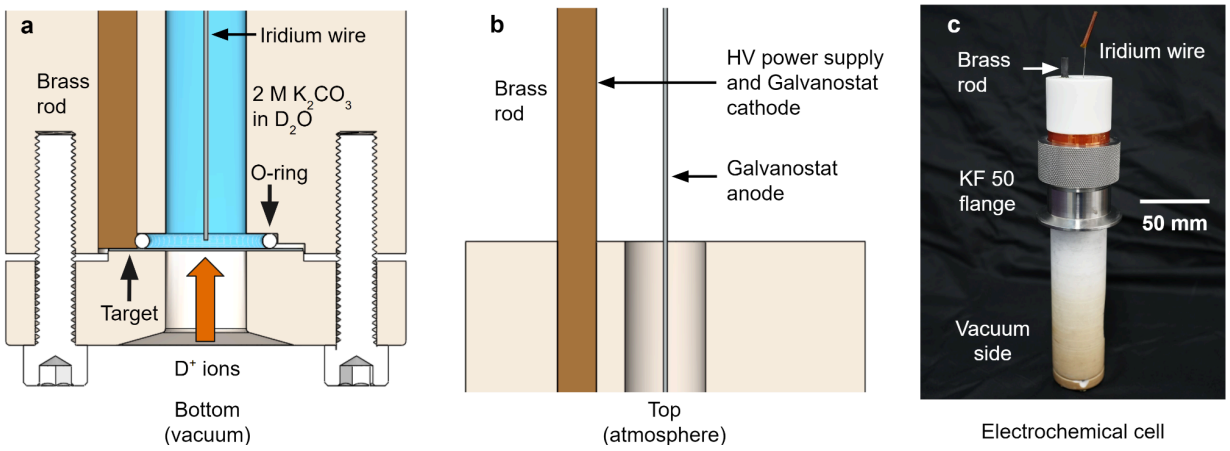

Supplementary Fig. 16: The Thunderbird Reactor electrochemical cell. a, Cross sectional schematic of the bottom of the electrochemical cell. **b,** Cross sectional schematic of the top of the electrochemical cell. **c,** The electrochemical cell is connected to the vacuum chamber via a KF 50 flange. The electrochemical cell is designed to separate the vacuum side and the atmospheric pressure side, and is used to bridge the electrochemical reaction and the nuclear fusion reaction. The vacuum side of the Pd target is bombarded by 30 keV D^+ ions, which is where the nuclear fusion reaction occurs.

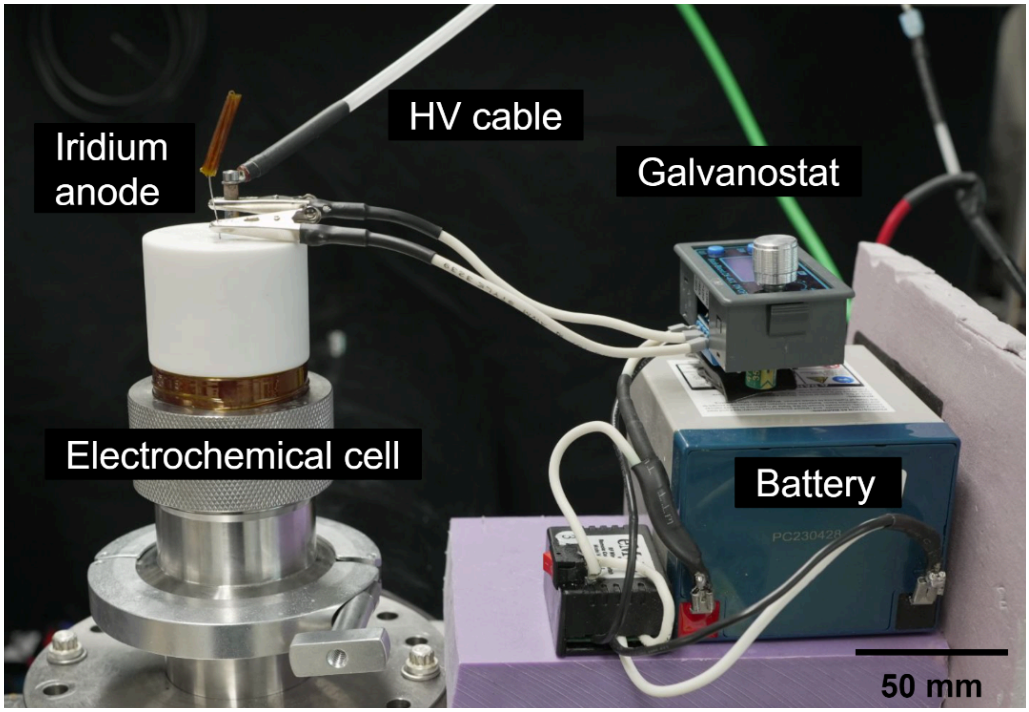

Supplementary Fig. 17: Electrochemical cell components in the Thunderbird Reactor. The Pd target is connected to the high-voltage power supply and the cathode of the galvanostat through a brass rod, while the Ir wire is connected to the anode of the galvanostat. The entire galvanostat operates at a potential of 12 V. To ensure safe operation, a battery powers the galvanostat, and a remote control is used to trigger it.

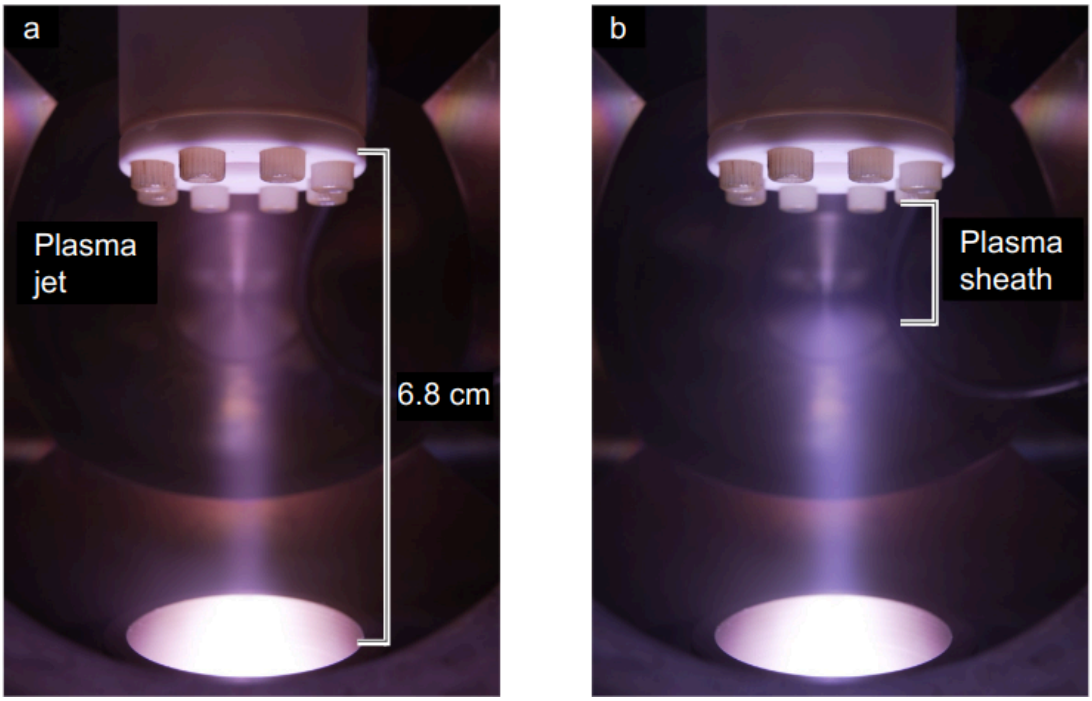

Supplementary Fig. 18: Photographs of the plasma in the vacuum chamber. a, The deuterium plasma jet generated by the plasma thruster engulfs the target material, but the nuclear fusion experiment has not yet started. **b,** When a negative high voltage is applied to the target, a plasma sheath is generated. Deuterium ions are then accelerated by the sheath voltage and injected into the target, initiating nuclear fusion reactions.

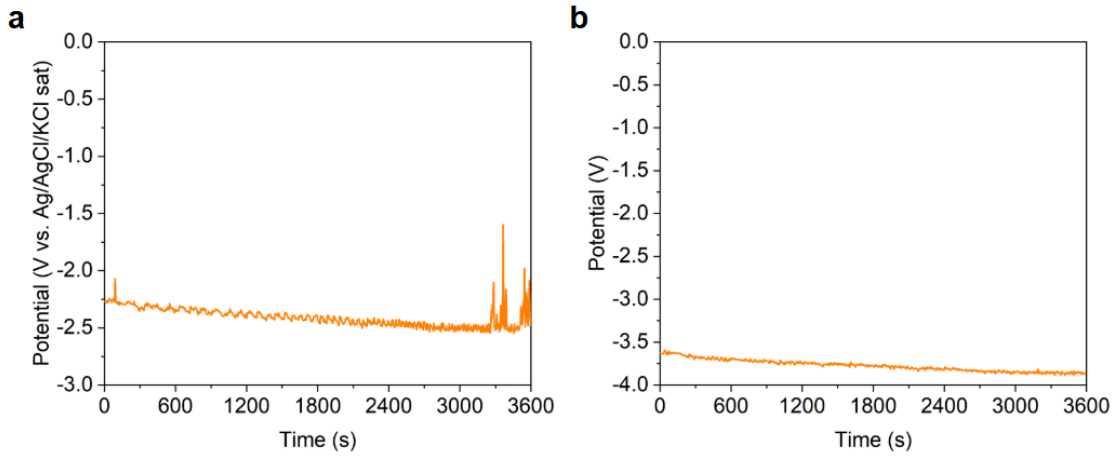

Supplementary Fig. 19: Electrochemistry in the Thunderbird Reactor. a, The potential of the Pd cathode during a constant current electrolysis at 200 mA. **b,** The cell voltage between the Pd cathode and Ir anode during a constant current electrolysis at 200 mA. For these measurements the electrochemical cell detached from the Thunderbird Reactor was set up with a three electrode system of a palladium cathode/target, iridium wire anode and Ag/AgCl/KCl_{sat} reference electrode. All electrochemistry was conducted on a Metrohm Autolab PGSTAT302N potentiostat.

References

1. Schirber, J. E. & Morosin, B. Lattice constants of \beta-PdH_x and \beta-PdD_x with x near 1.0. *Phys. Rev. B Condens. Matter* **12**, 117–118 (1975).
2. Marquardt, N. Introduction to the principles of vacuum physics. *https://inspirehep.net › literaturehttps://inspirehep.net › literature* (1999).
3. Kentish, S. E., Scholes, C. A. & Stevens, G. W. Carbon Dioxide Separation through Polymeric Membrane Systems for Flue Gas Applications. *Recent Patents on Chemical Engineering* **1**, 52–66 (2008).
4. Tabata, T. & Shirai, T. Analytic cross sections for collisions of h+, h2+, h3+, h, h2, and h− with hydrogen molecules. *At. Data Nucl. Data Tables* **76**, 1–25 (2000).
5. Yoon, J.-S. *et al.* Cross sections for electron collisions with hydrogen molecules. *J. Phys. Chem. Ref. Data* **37**, 913–931 (2008).
6. Stankovic, M. D., LeSage, N. E., Sperryn, J. F., Kurimoto, A. & Berlinguette, C. P. Electrochemical Hydrogenation of a Liquid Organic Hydrogen Carrier Using a Pd Membrane Reactor. *ACS Energy Letters* **0**, 4459–4464 (2024).
7. Singha Hazari, A., Frisch, M. L., Wen, Y., Stankovic, M. D. & Berlinguette, C. P. Electrolytic conversion of Nitro compounds into amines in a membrane reactor. *J. Am. Chem. Soc.* (2024) doi:10.1021/jacs.4c07847.
8. *CoMPASS User Manual*. https://www.caen.it/products/compass/ (2024).
9. Norsworthy, M. A. *et al.* Light output response of EJ-309 liquid organic scintillator to 2.86–3.95 MeV carbon recoil ions due to neutron elastic and inelastic scatter. *Nucl. Instrum. Methods Phys. Res. A* **884**, 82–91 (2018).
10. Enqvist, A., Lawrence, C. C., Wieger, B. M., Pozzi, S. A. & Massey, T. N. Neutron light output response and resolution functions in EJ-309 liquid scintillation detectors. *Nucl. Instrum. Methods Phys. Res. A* **715**, 79–86 (2013).
11. Safari, M. J. Differentiation method for Compton edge characterization in organic scintillation detectors. *Radiation Physics & Engineering* **1**, 9–16 (2020).
12. Chen, J. 40K. *Nucl. Data Sheets* **140**, (2017).
13. Kim, C., Yeom, J.-Y. & Kim, G. Digital n-γ Pulse Shape Discrimination in Organic Scintillators with a High-Speed Digitizer. *J. Radiat. Prot. Res* **44**, 53–63 (2019).
14. Brooks, F. D. DEVELOPMENT OF ORGANIC SCINTILLATORS. *NUCLEAR*

INSTRUMENTS AND METHODS **162**, 477–505 (1979).

15. Nakhostin, M. *Signal Processing for Radiation Detectors*. (John Wiley & Sons, 2017).
16. Zaitseva, N. *et al.* Plastic scintillators with efficient neutron/gamma pulse shape discrimination. *Nucl. Instrum. Methods Phys. Res. A* **668**, 88–93 (2012).
17. B. Baramsai, B.M. Steinetz, L. Forsley, R.E. Martin, P.B. Ugorowski, M.D. Becks, T.L. Benyo, A. Chait, R.C. Hendricks, G.C. Fralick, N. Penney, V. Pines, M. Pines, C.E. Sandifer II. *Fast Neutron Spectroscopy with Organic Scintillation Detectors in a High-Radiation Environment*. https://www1.grc.nasa.gov/wp-content/uploads/TM-20205008493-Fast-Neutron-Spectroscopy-with-Organic-Scintillation-Detectors-in-a-High-Radiation-Field.pdf (2020).
18. Bai, H. *et al.* Calibration of an EJ309 liquid scintillator using an AmBe neutron source. *Nucl. Instrum. Methods Phys. Res. A* **863**, 47–54 (2017).
19. Andrews, M. T., Bates, C. R., Pinilla, M. I., McKigney, E. A. & Sood, A. Development of validated detector models with MCNP® and DRiFT. in *2017 IEEE Nuclear Science Symposium and Medical Imaging Conference (NSS/MIC)* (IEEE, 2017). doi:10.1109/nssmic.2017.8533080.
20. Allison, J. *et al.* Recent developments in Geant4. *Nucl. Instrum. Methods Phys. Res. A* **835**, 186–225 (2016).
21. Allison, J. *et al.* Geant4 developments and applications. *IEEE Trans. Nucl. Sci.* **53**, 270–278 (2006).
22. Agostinelli, S. *et al.* Geant4—a simulation toolkit. *Nucl. Instrum. Methods Phys. Res. A* **506**, 250–303 (2003).
23. Eriksson J., E. al. Calculating fusion neutron energy spectra from arbitrary reactant distributions. *Computer Physics Communications* (2015) doi:10.1016/j.cpc.2015.10.010.
24. Bai, H. *et al.* Simulation of the neutron response matrix of an EJ309 liquid scintillator. *Nucl. Instrum. Methods Phys. Res. A* **886**, 109–118 (2018).
25. Andrews, M. T., Bates, C. R., Pinilla, M. I., McKigney, E. A. & Sood, A. Development of Validated Detector Models with MCNP® and DRiFT. in *2017 IEEE Nuclear Science Symposium and Medical Imaging Conference (NSS/MIC)* 1–3 (IEEE, 2017).
26. Matzke, M. *Unfolding of Pulse Height Spectra: The HEPRA Program System*. (Physikalisch-Technische Bundesanstalt, 1994).

27. Steinetz, B. M. *et al.* Novel nuclear reactions observed in bremsstrahlung-irradiated deuterated metals. *Phys. Rev. C.* **101**, (2020).
28. Ziegler, J. F. RBS/ERD simulation problems: Stopping powers, nuclear reactions and detector resolution. *Nucl. Instrum. Methods Phys. Res. B* **136-138**, 141–146 (1998).
29. Knoll, G. F. *Radiation Detection and Measurement*. (John Wiley & Sons, 2000).
30. Paff, M. G., Clarke, S. D. & Pozzi, S. A. Organic liquid scintillation detector shape and volume impact on radiation portal monitors. *Nucl. Instrum. Methods Phys. Res. A* **825**, 31–39 (2016).